



HAL
open science

Mechanical behavior of SiC/SiC composites reinforced with new Tyranno SA4 fibers: Effect of interphase thickness and comparison with Tyranno SA3 and Hi-Nicalon S reinforced composites.

James Braun, Cédric Sauder

► To cite this version:

James Braun, Cédric Sauder. Mechanical behavior of SiC/SiC composites reinforced with new Tyranno SA4 fibers: Effect of interphase thickness and comparison with Tyranno SA3 and Hi-Nicalon S reinforced composites.. Journal of Nuclear Materials, 2021, 558, pp.153367. 10.1016/j.jnucmat.2021.153367 . cea-03746265

HAL Id: cea-03746265

<https://cea.hal.science/cea-03746265>

Submitted on 5 Aug 2022

HAL is a multi-disciplinary open access archive for the deposit and dissemination of scientific research documents, whether they are published or not. The documents may come from teaching and research institutions in France or abroad, or from public or private research centers.

L'archive ouverte pluridisciplinaire **HAL**, est destinée au dépôt et à la diffusion de documents scientifiques de niveau recherche, publiés ou non, émanant des établissements d'enseignement et de recherche français ou étrangers, des laboratoires publics ou privés.

Mechanical behavior of SiC/SiC composites reinforced with new Tyranno SA4 fibers: Effect of interphase thickness and comparison with Tyranno SA3 and Hi-Nicalon S reinforced composites.

James Braun^a, Cédric Sauder^a.

^a Université Paris-Saclay, CEA, Service de Recherches Métallurgiques Appliquées, F-91191, Gif-sur-Yvette, France

Corresponding author:

James Braun
P33 – Bat. 460
CEA Saclay
91191 Gif-Sur-Yvette Cedex
France
james.braun@cea.fr

Keywords: Silicon carbide ; Ceramic Matrix Composites (CMCs) ; Mechanical properties ; Fiber.

Abstract

The development and availability of a new 3rd generation SiC fiber, the Tyranno SA4 (SA4), are promising for the processing of higher neutron and/or corrosion resistant SiC/SiC composites. Despite its promising properties, especially the higher crystallinity and thermal conductivity than the Hi-Nicalon S fiber, the previous Tyranno SA3 (SA3) reinforcement leads to low damage tolerant SiC/SiC composites, restraining its use as a reinforcement. This is the consequence of very high interfacial shear stress, whatever the pyrocarbon interphase thickness. In this work, tubular samples were produced with both reinforcements and with two different pyrocarbon interphase thicknesses for tensile mechanical characterizations to access the potential benefit of the new SA4 fibers. The tensile mechanical properties of SA4 composites are highly enhanced compared to SA3 composites. The low damage tolerance drawback of SA3 composites is solved with higher failure strain for SA4-based composites. Tensile mechanical tests also highlight an unusual influence of pyrocarbon interphase thickness on the composites tensile modulus and proportional limit stress. The thinner interphase (≈ 60 nm) is the most interesting for repeatable mechanical properties and induces high proportional limit stress. Unloading – reloading cycles during tensile mechanical tests also highlight the benefit of this new fiber compared to Hi-Nicalon S. This work demonstrates that the substitution of SA3 by the new SA4 SiC fiber reinforcement in the processing of SiC/SiC composites is a great opportunity for the ceramic matrix composites development and especially for nuclear applications.

1. Introduction

For decades, SiC-based materials and especially SiC/SiC composites have been considered as potential candidates for nuclear applications [1–4]. In fission reactors, core applications, like cladding or control rods, have widely been studied for Gas-cooled Fast Reactors (GFR), Very High Temperature Reactors (VHTR) or Light Water Reactors (LWR) [1]. The benefits of the SiC phase are mainly its high thermal conductivity, high mechanical resistance up to high temperature, chemical inertness and low neutron absorption with high neutron irradiation resistance [1]. Only the 3rd generation SiC fibers, Hi-Nicalon S (HNS) and Tyranno SA3 (SA3), known as “stoichiometric fibers”, are supposed to be used as SiC/SiC composites reinforcement for nuclear applications [1,2]. In this framework, the pyrocarbon (PyC) is the most suited interphase material, although it must be as thin as possible to maximize the neutron irradiation resistance at high dose [5–7]. PyC interphase is also resistant to hydrothermal corrosion in LWR environments [8]. Finally, Chemical Vapor infiltration (CVI) is the best choice to manufacture the SiC matrix for nuclear applications. This process leads to highly crystalline and pure SiC phase, resulting in irradiation stable SiC matrix [9–11]. Moreover, the CVD/CVI SiC is the most corrosion resistant from all the processes dedicated to densification of composites. For example, CVD SiC is at least an order of magnitude more resistant to hydrothermal corrosion in LWR environment than the NITE process [12].

SA3 and HNS fibers properties are quite similar, even if SA3 fibers and SA3 composites have higher thermal conductivity due to higher crystallinity (larger grain size of SA3 fibers) [13,14] and better thermal stability [15,16], which are mainly the consequence of the SA3 fibers higher processing temperature. The major drawback of manufacturing composites with SA3 reinforcement is the resulting low damage tolerance compared to HNS composites. Regardless of the PyC interphase thickness, tensile failure strains are always below 0.3% for SA3 composites. Higher tensile failure strains for SA3 minicomposites (similar to HNS minicomposites one) have already been reported with 150 nm thick PyC interphase, but strong discrepancies from one sample to another appeared [17–22]. The reason for such low ductility is a very strong Interfacial Shear Stress (ISS), leading to a stronger Fiber/Matrix (F/M) bonding in SA3 composites than in HNS composites [23–26]. For SA3 composites, ISS is reported to be an order of magnitude higher than the HNS-based composites one [27]. The reason is not completely understood yet, even if the authors suspect that the extreme surface chemical composition and/or higher surface roughness of the SA3 fiber play key roles [20,21,27,28].

This low damage tolerance as well as the HNS fiber earlier availability explain why HNS-reinforced composites have widely been studied for nuclear applications in comparison with SA3 composites [29]. Recent studies [7,29–33] clearly highlight the degradation of HNS composites after neutron irradiation at intermediate temperature (300-800°C), although CVD SiC (similar to the SiC matrix in SiC/SiC

composites) behaves well in the same conditions. A strong degradation of F/M bonding after irradiation occurs and, in the worst case (low irradiation temperatures), a complete loss of bonding between the fiber and the matrix is observed. The PyC sensitivity to neutron irradiation is the first reason of ISS degradation [7,32] but recent studies also highlight that the HNS fiber is clearly damaged at low irradiation temperature and/or for high doses [7,29,32]. Therefore, after irradiation, HNS fiber shrinkage is observed and a decrease in its strength is believed to occur. These last results question the use of HNS fiber as reinforcement in specific nuclear applications (i.e. high dose/low temperature). Moreover, additional issues have arose from the hydrothermal corrosion behavior in representative LWR environment of the HNS fiber, even if this phenomenon highly depends on the chemistry [8,34]. The HNS fiber has a poor hydrothermal corrosion resistance in comparison with CVD SiC, characterized by a significant dissolution rate. This can be explained by HNS fiber small grain size compared to CVD SiC. Indeed, influence of SiC crystallinity on the hydrothermal corrosion resistance has been proven [35–37], even if additional factors (ex: electrical resistivity) also play a role [36].

As HNS fiber does have limitations for nuclear applications at intermediate temperature and/or high dose, especially in a LWR environment, the need of another nuclear compatible SiC fiber is highly needed. Irradiation stability at intermediate temperature (300 - 600°C) of SA3 fibers and/or SA3 composites are promising [7,29,32]. The shrinkage and loss of carbon phase observed for the HNS fiber are not observed for SA3 fiber under ion irradiation at 300°C up to very high doses (> 50 dpa) [32]. After neutron irradiation at 600°C up to 44 dpa [7], SA3 composites are more resistant than HNS composites even if a decrease in strength is also observed. The irradiation resistance of SA3-based composites is promising but their mechanical behavior needs to be improved for their use in structural applications. Indeed, despite 20 years of research, highly damage tolerant SA3-reinforced composites have never been fabricated. Hence, the availability of a new SiC fiber, the Tyranno SA4 (SA4), has particularly aroused interest and could be a great opportunity to solve this issue.

In the present work, the SA3 and the new SA4 fibers (both supplied by Ube industries) were used as reinforcements of specific 2D SiC/SiC cladding sections produced by filament winding and CVI densification with two different PyC interphase thicknesses. Up to now, no data on the mechanical behavior of SA4 SiC/SiC composites is noted. Tensile mechanical behavior of tubular specimens with different PyC interphase thicknesses are then assessed. Damage evolution and friction mechanisms are discussed, based on the analysis of specific unloading-reloading cycles. Finally, similar HNS-reinforced cladding samples allows comparison and discussion about the influence of these reinforcements on the SiC/SiC composites mechanical behavior.

2. Materials and method

2.1. SiC/SiC cladding processing

3rd generation Tyranno SA3, Tyranno SA4 (Ube industries) and Hi-Nicalon Type S (NGS Advanced Fibers Co.) fibers were used as SiC/SiC cladding reinforcement. The fibers properties, provided by each suppliers, are summarized in **Table 1**. Detailed characterizations of SA3 and HNS fibers were previously done [38,39]. SEM micrographs of the cross sections of HNS, SA3 and SA4 fibers are presented in **Fig. 1** for comparison.

Table 1

Fibers main characteristics provided by each suppliers.

Fiber	SA3	SA4	HNS
Lot number / Type	SA3-S1F08PX	SA4-08PW	539341
Young's modulus E_f (GPa)	368	399	371
Strength (GPa)	2.24	3.08	3.2
Density (g/cm ³)	3.1	3.09	3.02
Diameter (μm)	10	10	13
Sizing content (%)	0.59	0.78	0.9
Tex (g/km)	175	176	198

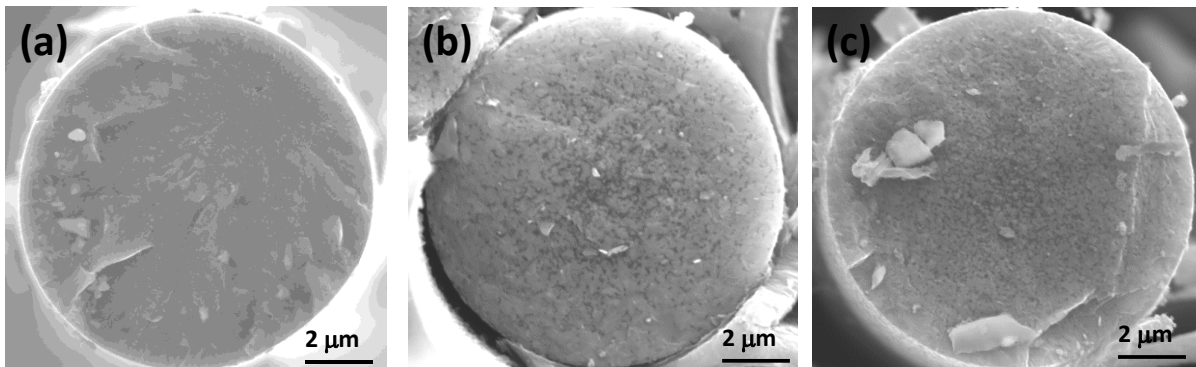


Fig. 1. HNS (a), SA3 (b) and SA4 (c) fibers SEM cross sections.

The SA4 fiber grain size and carbon content at the core level have been reduced in comparison with SA3 fiber (**Fig. 1**). According to the manufacturer, this lower grain size do not lead to a thermal conductivity decrease. The main improvement from SA3 to SA4 fiber is the much higher tensile strength of SA4 fiber ($\approx 40\%$), similar to the HNS one. The manufacturer also announces that SA4 tows

flexibility and friction resistance are enhanced compared to SA3. Therefore, weavability should be improved.

These fibers were used to manufacture SiC/SiC cladding composites made of a 3 layers structure, each made of $\pm 45^\circ$ filament wound structure, to meet the tubes dimensional tolerance. The fiber structure is processed on a silica mandrel for specific criteria, explained in [40]. During this process, largely lower fiber fluff situation occurred with SA4 and HNS, which confirms that SA4 weavability is highly improved compared to SA3.

Chemical Vapor Infiltration (CVI) was employed for the PyC interphase and SiC matrix depositions. SA3 and SA4 fibrous structures were densified in the same batch with two pyrocarbon interphase thicknesses (Fiber/PyC_{thickness}/SiC). A highly anisotropic PyC texture was chosen to optimize F/M bonding [21]. As SA4 is a new fiber without any hindsight, the same densification process without the PyC interphase deposition was applied (SA4/SiC). The SA3/SiC composite (i.e. without interphase) was not produced because a previous study [21] clearly demonstrated that this kind of composite has a brittle mechanical behavior with very low ultimate tensile strain (0.05%). After densification, to obtain better dimensional tolerances, the internal and external surfaces were grinded by running-in and centerless processes, respectively.

The HNS composite used for comparison was previously processed in the same way with an analogous low thickness PyC interphase (HNS/PyC_{thickness}/SiC). The only difference with the SA3 and SA4 composites is that further SiC densification with a final grinding step was added to reduce the level of porosity to a very low level. Typical cladding composite (200 mm length and ~10 mm diameter) produced is presented **Fig. 2**.

The fiber and matrix volume fractions (resp. V_f and V_m) cannot be precisely measured because of the grinding steps. From experience [40], $V_f = V_m$ is believed to be a good approximation and will be used within this work. Cylindrical alumina standards and an optical profilometer (TESA SCAN 52 Technology) were employed to determine the internal and external average diameters along the length of the tubes, respectively. A Zeiss Evo Scanning Electron Microscope (SEM) was used for interphase thickness measurements. Estimation of the PyC volume fraction (V_i) was calculated considering a uniform deposition on the fibers. The porosity volume fraction (V_p) was determined from the fiber, interphase and matrix theoretical densities. Characteristics of the manufactured composites are presented in **Table 2**.



Fig. 2. SiC/SiC composites cladding as processed.

Table 2

SiC/SiC cladding characteristics mean values (standard deviation).

Sample type	PyC thickness (nm)	Density (g/cm ³)	V_f and V_m (%)	V_i (%)	V_p (%)
SA4/SiC	0	2.84 (0.04)	45.5	0	9.0 (1.1)
SA4/PyC _{60nm} /SiC	60 (10)	2.78 (0.02)	44.3	1.1	10.3 (0.6)
SA4/PyC _{250nm} /SiC	250 (50)	2.76 (0.06)	42.6	4.5	10.3 (0.6)
SA3/PyC _{60nm} /SiC	60 (10)	2.66 (0.05)	43.0	1.0	13.0 (1.3)
SA3/PyC _{250nm} /SiC	250 (29)	2.66 (0.08)	41.3	4.4	13.0 (2.1)
HNS/PyC _{80nm} /SiC	80 (20)	2.94 (0.01)	47.0	1.1	4.9 (0.3)

2.2. Thermally induced residual stress

Thermally induced residual stresses in each phase (i.e. fiber, interphase and matrix) were determined considering a single fiber and concentric cylinders of interphase and matrix [41]. Good correlations for minicomposites [27] and 2D composites [40] tensile mechanical behavior were previously obtained with this model. The thermal expansion coefficients, Young's modulus and Poisson's ratio evolutions of each phase (fiber, interphase and SiC) as a function of temperature used in this model are already reported in [27], except for the SA4 fiber, which still needs to be assessed. The calculated residual thermal stresses of the processed SA3 and HNS composites are presented in **Fig. 3**. The level of residual thermal stresses in the matrix and the fiber are quite low for all the composites, preventing any degradation (matrix cracks or fiber failure) during the cool down from the CVI step ($\approx 1000^\circ\text{C}$). The fiber is in slight tension in each direction. The matrix is under weak tension in radial direction and under compression in circumferential and longitudinal directions. The interphase is under tension in radial and circumferential directions and under compression in longitudinal direction. When the PyC

thickness increases, slightly higher thermal residual stresses are noted. Finally, residual thermal stresses are similar whatever the fiber nature for similar PyC interphase thicknesses.

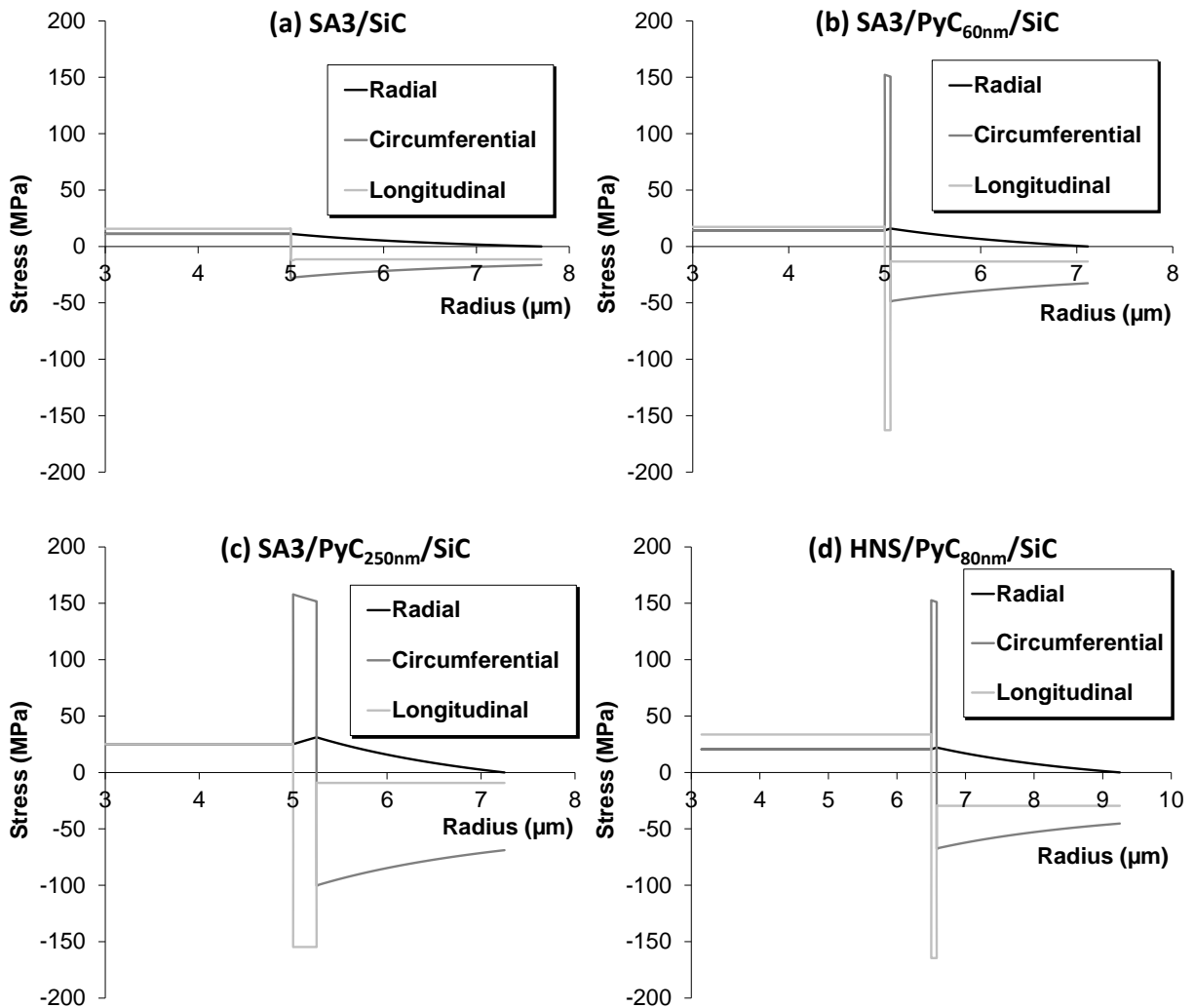


Fig. 3. Radial, circumferential and longitudinal residual thermal stresses calculated in microcomposite with fiber and matrix equivalent fractions for (a) SA3/SiC, (b) SA3/PyC_{60nm}/SiC, (c) SA3/PyC_{250nm}/SiC and (d) HNS/PyC_{80nm}/SiC.

2.3. Mechanical characterizations

SiC/SiC cladding were cut down to 65mm in length to perform 3 uniaxial tensile tests for each type of composites, described in the ISO 20323 standard [42] and shown in Fig. 4. 3M scotch-Weld™ 9323 B/A epoxide structural glue was used to fix the test specimens on end collars on the mechanical testing machine (Instron 2404). The longitudinal and diametral strains were measured with a 25 mm EPSILON 3442-010M-010M-ST (± 1 mm course) and a MTS 632.19F-20 (± 1 mm course) sensors, respectively. Matrix multicracking and microstructure coupling were monitored with an Acoustic Emission (AE) sensor (90 – 295 kHz), fixed on the upper end collar. Only events above 50 dB in intensity were taken

into account to avoid noise perturbations. The AE evolution during tensile tests is represented by AE/AE_{max} (AE and AE_{max} are the number of events for a given level of stress reached and the number of events at sample fracture, respectively). Up to 9 unloading – reloading cycles were conducted at strain rates ranging from 0.05 to 0.2 mm/min. Full details about the testing procedure can be found in [40].

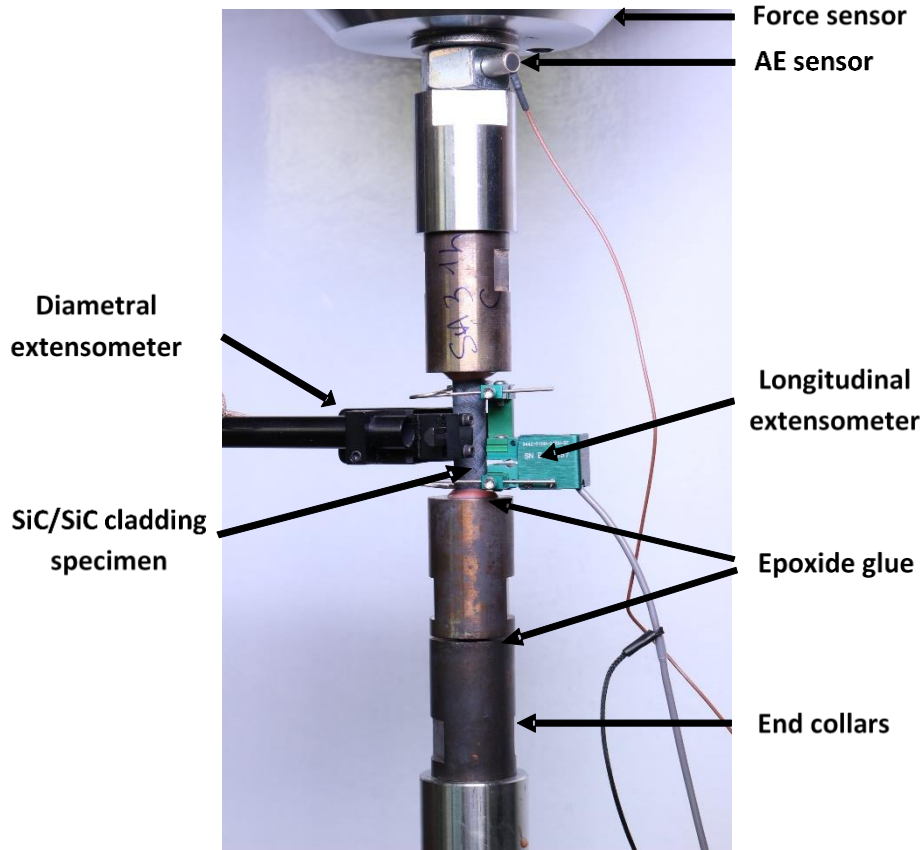


Fig. 4. Experimental device employed for tensile tests.

The initial Young's modulus (E_0) is defined as the slope of the initial linear portion of the stress-strain curve during a tensile test. In CMC, the onset of nonlinearity, i.e. Proportional Limit (PL), is often associated with the macroscopic manifestation of the first matrix cracking (or crack opening), onset of the matrix multicracking process (cumulative damage). In some CMC, there is evidence that damage cumulative process may begin before the PL [43]. Moreover, the linear region in CMC is not always obvious [40]. Five different procedures have previously been compared [43]. Even if there is no real consensus on the most suited method for Proportional Limit Stress (PLS) determination, the deviation from linearity method is the most consistent and least variable. In this method, PLS is determined as the stress at which there is a specified percent deviation ($\%dev$) from the stress calculated from the elastic relation, $\sigma = E_0\varepsilon$, such that (**Eq. (1)**):

$$\%dev = 100 \left[\frac{(E_0 \varepsilon_i) - \sigma_i}{\sigma_i} \right] \quad (1)$$

Where σ_i and ε_i are the corresponding stress and strain, respectively, and E_0 is the initial elastic modulus. The PLS is determined, such that $PLS = \sigma_i$ when $\%dev$ exceeds the specified value when evaluating increasing σ_i and ε_i , starting from zero. This method is applied in this study for determination of PLS with $\%dev = 10\%$ ($PLS_{10\%dev}$). The first significant AE signal is also used for the determination of PLS (PLS_{AE}).

The reduced modulus (E/E_0), the area of the cycles (ΔW) and anelastic residual strains after unloading (ε_r) are determined from the unloading – reloading cycles [44,45]. E , the longitudinal elastic modulus, is determined by measuring the slope of the line passing through the summit of the cycle ($\sigma_{max}, \varepsilon_{max}$) and the median point of the cycle for a $\sigma_{max}/2$ stress [40,46]. The reduced modulus decreases as a function of the applied stress, reaching an asymptotic behavior, related to the fiber fraction in the mechanical solicitation direction and Young's modulus (**Eq. (2)** for a 2D plate composite solicited at a Φ angle towards the tows direction) [47]. E_f and V_f are the tow Young's modulus and the fiber volume fraction, respectively. Recently, authors highlighted that this formula seems also suitable for a $\pm 45^\circ$ angle tubular structure [40].

$$\lim_{\varepsilon \rightarrow \varepsilon_{max}} \frac{E}{E_0} = 0.5 \frac{E_f V_f}{E_0} (\cos^4 \Phi + \sin^4 \Phi) \quad (2)$$

3. Results

3.1. Tensile mechanical behaviors

The typical stress-strain curves along with the relative AE signal are presented in **Fig. 5** for each type of SiC/SiC cladding. SEM fracture surface observations are presented in **Fig. 6**. A compilation of typical tensile stress-strain curves of all composite type is presented (**Fig. 7**) for a better comparison and data are resumed in **Table 3**.

Mechanical tensile behavior of HNS composites corresponds to a low ISS composite mechanical behavior, whereas SA3 and SA4 composite have similar mechanical behaviors, corresponding to a high ISS composite mechanical behavior [48,49]. For HNS composites, pullout fibers are observed (**Fig. 5 (f)**). The debonding lengths, i.e. extracting from the matrix sheath, are quite high (from several dozen to hundreds of micrometers), featuring a moderate to low F/M bonding [20,21,27,40].

As previously observed [16,17,21,24,25,27], SA3 composites have low failure strains whatever is the PyC interphase thickness, even if thicker interphases lead to slightly higher failure strains up to 0.3%. Mechanical tensile behavior (**Fig. 7, Table 3**) of SA3 composite supports that a thicker PyC interphase

reduces the ISS [17,24], but this reduction do not strongly influence the tensile failure strain of these composites. No or very short pullout fibers (maximum debonding lengths of few micrometers) are observed on the SA3 composites fracture surfaces (**Fig. 5 (d)** and **(e)**), independently from the PyC interphase thickness, supporting a strong F/M bonding without debonding and or sliding after mechanical tensile tests [27].

The original result is that SA4 composites have largely higher failure strain than SA3 composites for an equal interphase thickness. Pullout fibers are observed on all SA4 composites (**Fig. 6**), even without a PyC interphase. Debonding lengths raise from few micrometers for SA4/SiC to few dozen micrometers for SA4/PyC_{60nm}/SiC and SA4/PyC_{250nm}/SiC. The PyC thickness influence on the mechanical behavior is similar to SA3 composites (**Fig. 6**), which is the consequence of a decrease of ISS.

Therefore, the composites Young's modulus is highly influenced by the interphase thickness even for low interphase volume fraction ($V_i \leq 5\%$). Finally, PLS is also highly influenced by the PyC interphase thickness.

Table 3

SiC/SiC cladding mechanical characteristics mean values (standard deviation).

Composites	Young's modulus (GPa)	Failure strength (MPa)	Longitudinal failure strain (%)	Diametral failure strain (%)	PLS _{10%dev}	PLS _{EA}
SA4/SiC	311 (4)	293 (15)	0.34 (0.13)	-0.043 (0.010)	187 (9)	152 (12)
SA4/PyC _{60nm} /SiC	283 (7)	296 (5)	0.75 (0.05)	-0.181 (0.043)	138 (2)	141 (12)
SA4/PyC _{250nm} /SiC	198 (26)	285 (19)	0.77 (0.10)	-0.223 (0.025)	105 (13)	112 (9)
SA3/PyC _{60nm} /SiC	284 (7)	228 (8)	0.14 (0.02)	-0.148 (0.013)	189 (4)	156 (14)
SA3/PyC _{250nm} /SiC	221 (22)	229 (5)	0.27 (0.05)	-0.027 (0.008)	142 (17)	112 (15)
HNS/PyC _{80nm} /SiC	263 (7)	288 (6)	0.98 (0.05)	-0.047 (0.018)	73 (3)	106 (2)

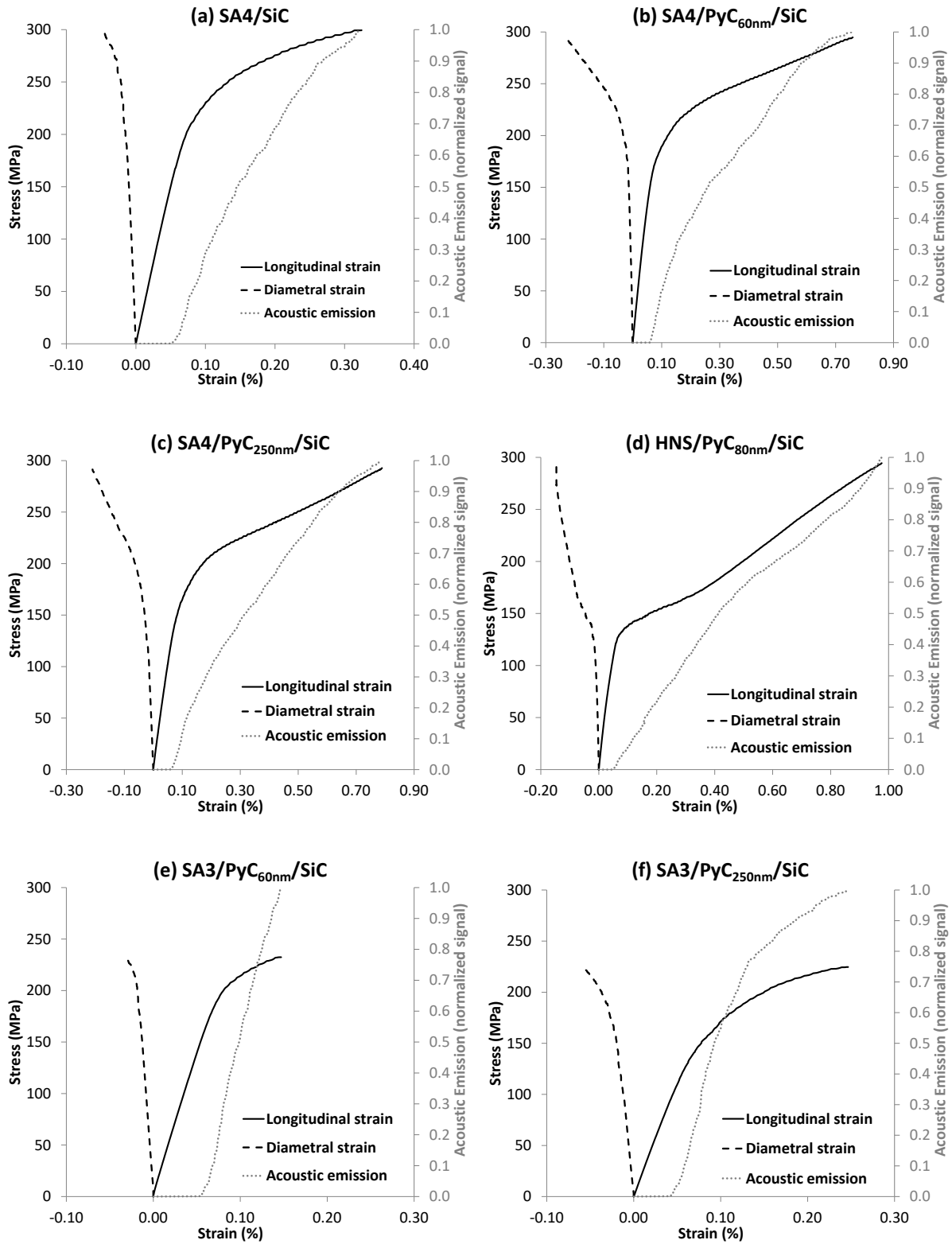


Fig. 5. Typical tensile stress-strain curves along with the evolution of normalized AE for each type of SiC/SiC cladding: **(a)** SA4/SiC, **(b)** SA4/PyC_{60nm}/SiC, **(c)** SA4/PyC_{250nm}/SiC, **(d)** HNS/PyC_{80nm}/SiC, **(e)** SA3/PyC_{60nm}/SiC and **(f)** SA3/PyC_{250nm}/SiC.

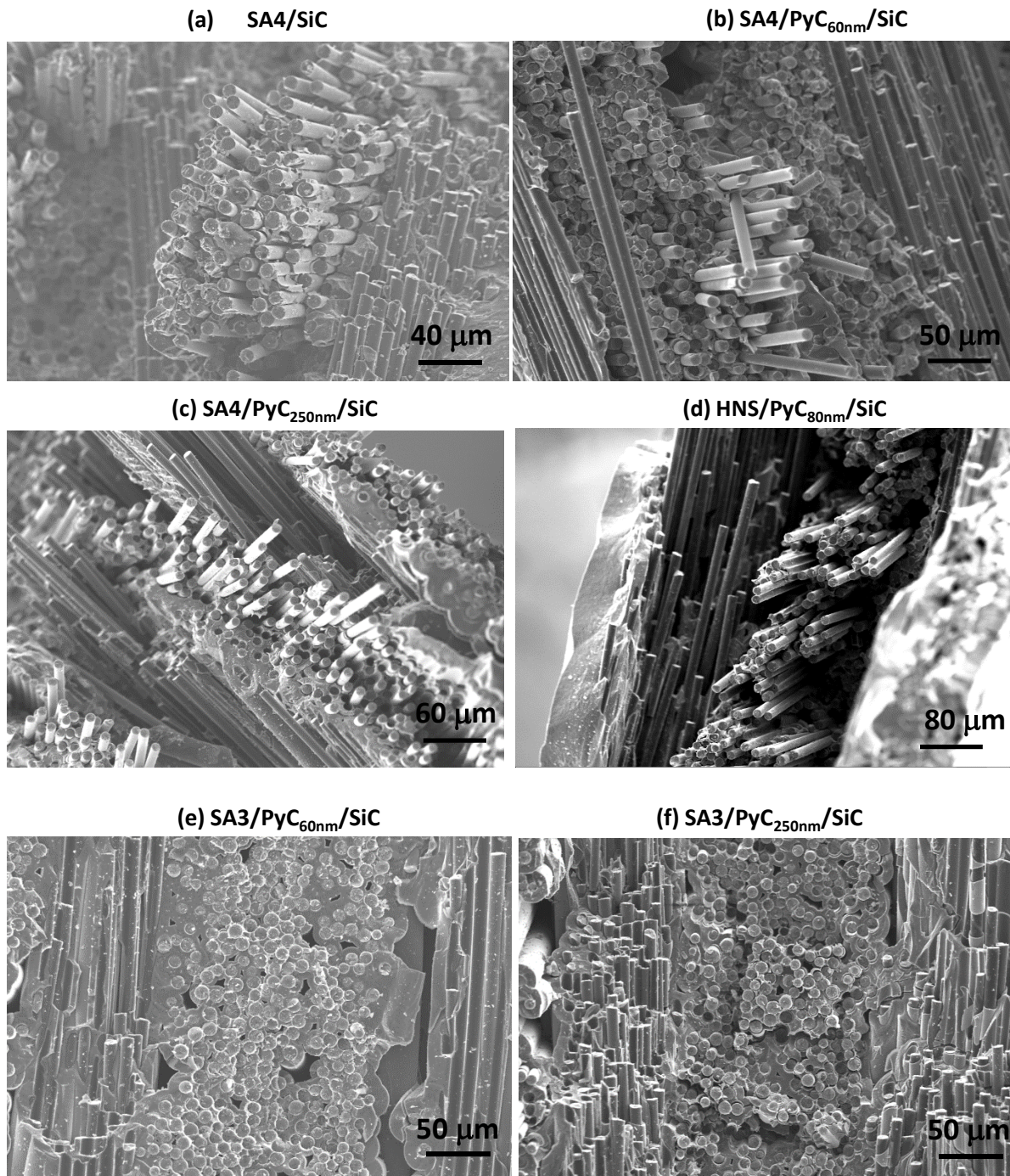


Fig. 6. Fracture surface after ultimate failure for each type of SiC/SiC cladding: (a) SA4/SiC, (b) SA4/PyC_{60nm}/SiC, (c) SA4/PyC_{250nm}/SiC, (d) HNS/PyC_{80nm}/SiC, (e) SA3/PyC_{60nm}/SiC, (f) SA3/PyC_{250nm}/SiC.

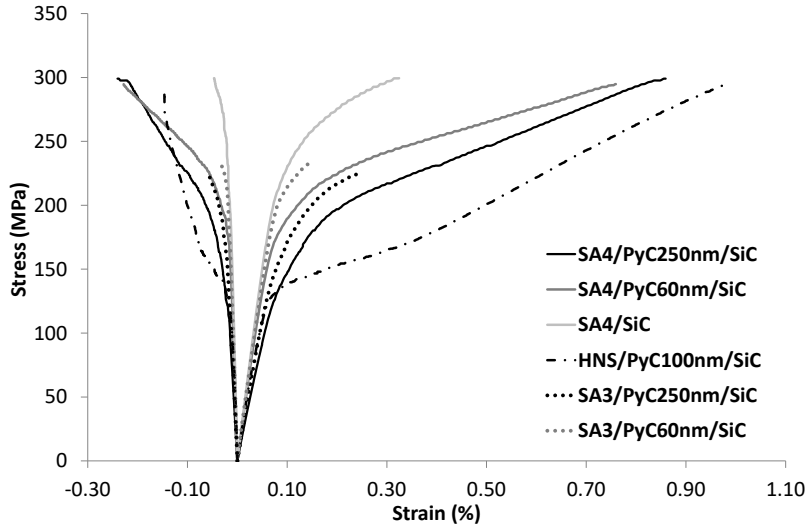


Fig. 7. Influence of the fiber type and the pyrocarbon interphase thickness on the tensile stress-strain behavior.

3.2. Unloading-reloading cycles analysis

A representative tensile stress-strain behavior (with unloading-reloading sequences) of each thin PyC interphase (60 nm for SA3 and SA4 composites and 80 nm for HNS composite, respectively) cladding composite is presented in **Fig. 8**. The evolution of reduced modulus (E/E_0), area of cycles (ΔW) and residual strain (ϵ_r) as a function of the maximum stress applied before unloading sequences is presented in **Fig. 9** for all the materials.

The evolution of E/E_0 (**Fig. 9 (a)**) is directly related to the fiber nature and the PyC interphase thickness. For a given stress, the reduced modulus decrease is stronger and reaches the saturation value (**Eq. (2)**) before 200 MPa for HNS reinforcement. This phenomenon was already observed for similar composites [40] and is the consequence of a low ISS in HNS composites. PLS measurements (**Table 3**) confirm this earlier degradation of composites (matrix cracking and/or opening of existing cracks) for HNS reinforcement than for SA3 and SA4 ones. Evolution of reduced modulus also clearly depends on the PyC interphase thickness. The thicker the interphase is, the earlier degradation (i.e. at lower stresses) of reduced modulus appears. The reduced modulus decrease is limited for SA3 fiber reinforcement, which is clearly related to very high ISS in these materials. Saturation of matrix multicracking is not observed for SA3 composites, whereas this saturation should take place just before the ultimate failure (≈ 300 MPa) for SA4 composites. To avoid possible fatigue degradation mechanisms at high stress, cycled tensile tests were not conducted at such high levels of damage.

The extended hysteresis loops area are characteristic of energy dissipated by sliding with significant fiber/matrix interface friction (**Fig. 8**). The hindrance of the crack closing after stress release is detected, including an apparent stiffness [50]. The higher area and residual strain at similar stress for

HNS composite (**Fig. 9 (b)** and **(c)**) is the consequence of the composite degradation as previously discussed.

Two contributions are extracted from the anelastic residual strain (ε_r), ε_T , the residual thermal strains generated following the high temperature processing (CVI) from the differences in the thermomechanical properties when the composites are brought to room temperature and ε_f , the partial irreversible sliding and mechanical hindrance of the cracks reclosing. ε_r , ε_T and ε_f are linked by **Eq. (3)** [44].

$$\varepsilon_r = \varepsilon_T + \varepsilon_f \quad (3)$$

ε_T is measured from the intersection of the stress-strain curves tangent at the end of the reloading step and the abscissa axis for each cycles. Moreover, all the tangents cross at the same point, corresponding to the axial thermal residual stress (σ_T) in the fibrous reinforcement after processing. Details on the procedure for determining σ_T and ε_T , as a function of stress level, is described in [40,44]. The values of σ_T measured for all cladding composites are presented in **Table 4** and compared with the values of longitudinal thermal residual stresses calculated in § 2.1.3 (**Fig. 3**). There is a good agreement between the measured values from tensile unloading-reloading and estimated values by microcomposite model (§ 2.1.3.). The evolution of ε_r , ε_T and ε_f as a function of the maximum stress reached before unloading sequences are presented in **Fig. 10** for the low interphase thickness SA4, SA3 and HNS cladding composites.

For HNS composite, a saturation of the thermal longitudinal strains occurs around 200 MPa, which confirms a saturation of the matrix multicracking at this stress level. The irreversible strains (ε_f) and anelastic residual strains (ε_r) also seem to tend to an asymptotic value over 200MPa. For SA3 and SA4 composites, no saturation is observed for any of residual strains even at 270 MPa. This confirms that their matrix multicracking saturation is not reached even at these very high stresses. Thermal residual and irreversible strains are higher for SA4 composites compared to SA3 composites. This is the consequence of higher axial thermal residual stresses in SA4 composites. Finally, anelastic strain is very low, almost negligible for SA4 composites, even at very high stresses. Effect of PyC interphase thickness (not represented) on SA3 and SA4 composites behavior is low and leads to weakly higher residual strains with the same global evolution (no saturation at high stress levels).

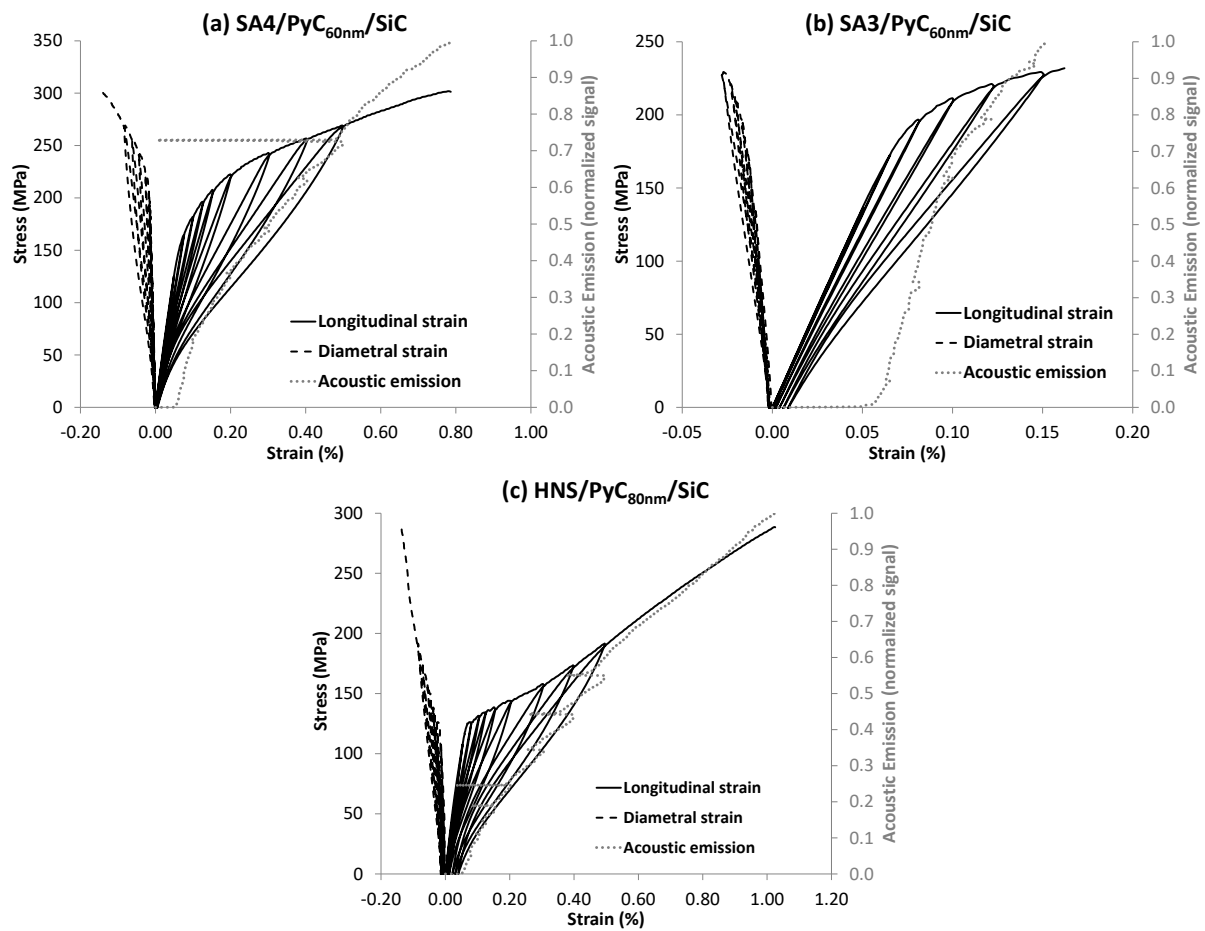


Fig. 8. Typical tensile stress-strain behaviors with unloading-reloading sequences with evolution of normalized AE signal for **(a)** SA4/PyC_{60nm}/SiC, **(b)** SA3/PyC_{60nm}/SiC and **(c)** HNS/PyC_{80nm}/SiC cladding composites.

Table 4

Comparison of σ_T measured through unloading-reloading sequences analysis with residual longitudinal stresses estimated with the model presented in § 2.1.3 for all cladding composites.

Composites	Axial thermal residual stress σ_T from unloading-reloading cycles analysis (MPa)	Longitudinal thermal residual stress estimated in § 2.1.3. (MPa)
SA4/SiC	50	-
SA4/PyC _{60nm} /SiC	60	-
SA4/PyC _{250nm} /SiC	55	-
SA3/PyC _{60nm} /SiC	22	17
SA3/PyC _{250nm} /SiC	34	25
HNS/PyC _{80nm} /SiC	33	34

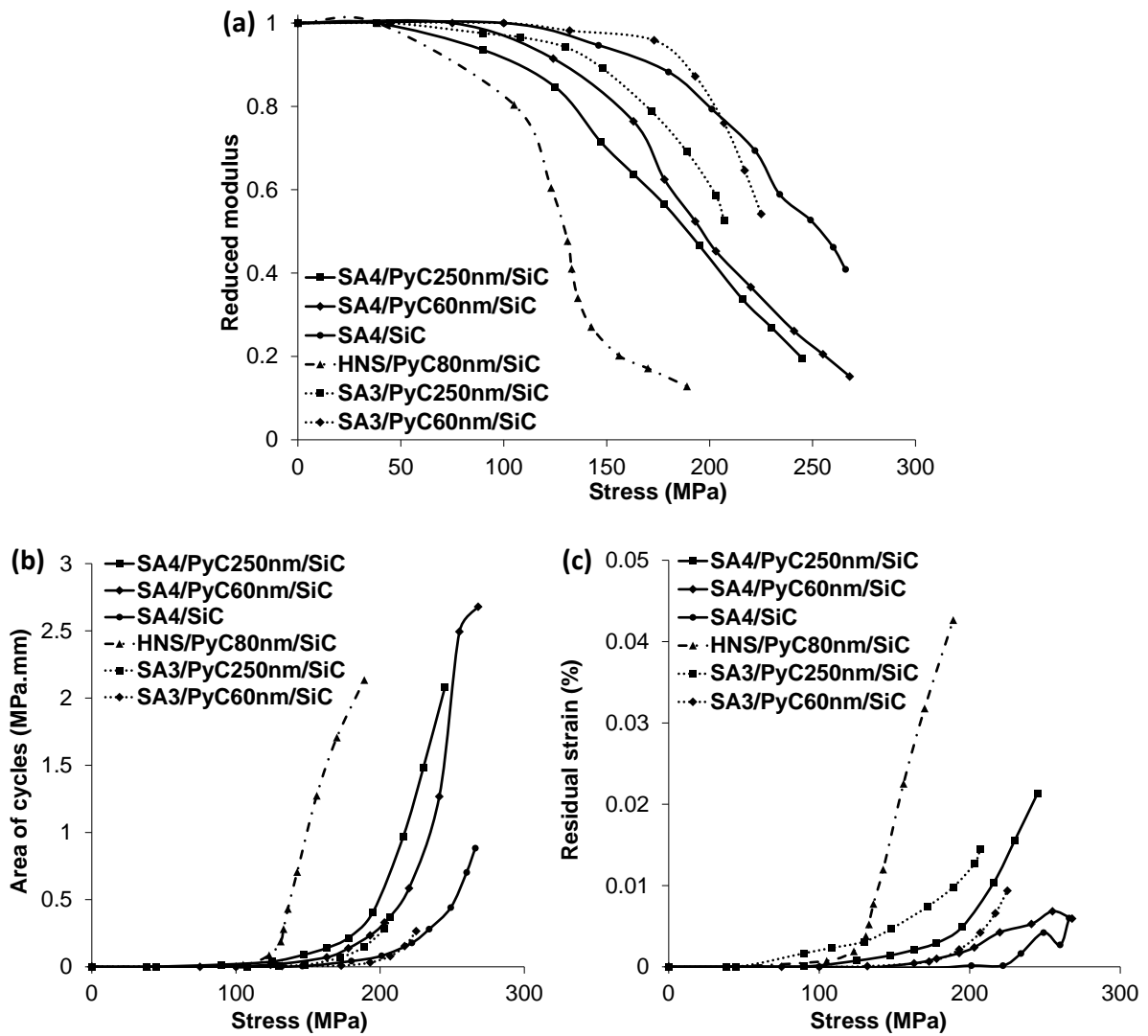
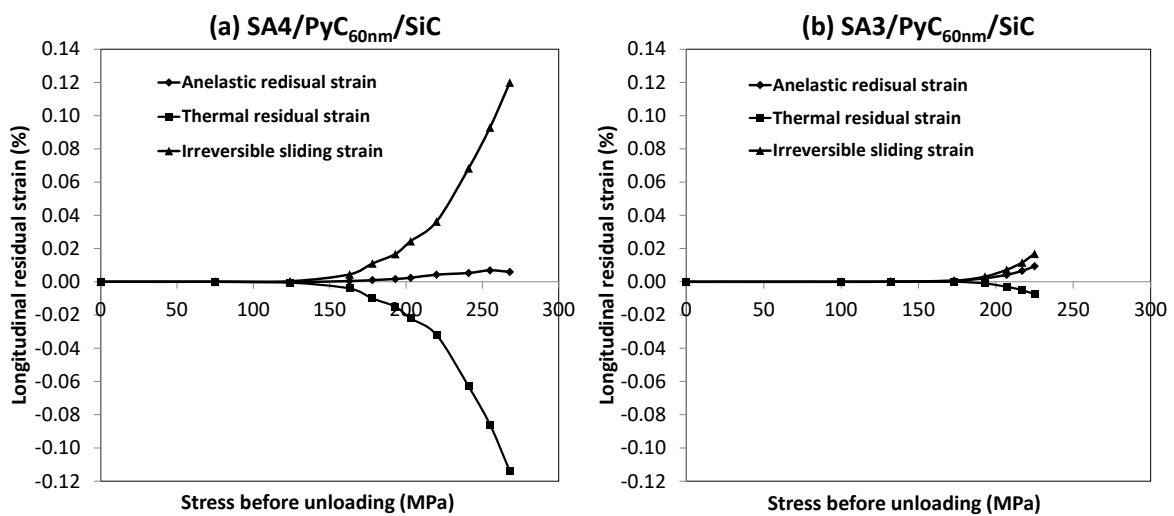


Fig. 9. Evolution of (a) the reduced modulus (E/E_0), (b) the area of cycles (ΔW) and (c) the residual strain (ϵ_r) as a function of the maximum applied stress reached before unloading for all cladding composites.



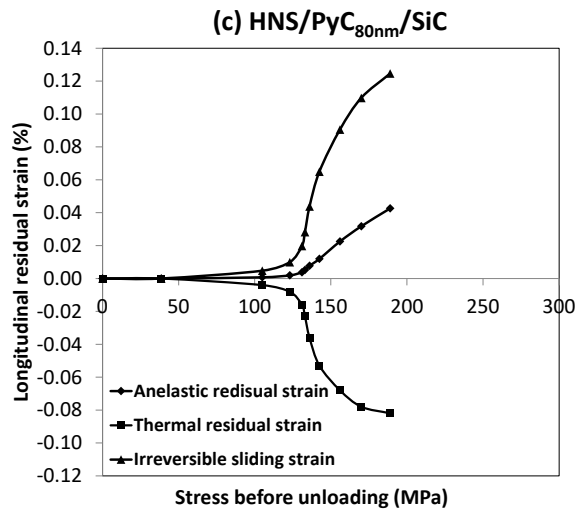


Fig. 10. Anelastic (ϵ_r), irreversible (ϵ_f) and thermal (ϵ_T) residual strains as a function of the stress reached before unloading for (a) SA4/PyC_{60nm}/SiC, (b) SA3/PyC_{60nm}/SiC and (c) HNS/PyC_{80nm}/SiC cladding composites.

4. Discussion

Mechanical behavior of composites highly depends on the ISS as previously predicted [48,49]. When the ISS increases (within the 5 – 200 MPa range), the failure strain tends to decrease, whereas the corresponding applied force increases. For low ISS values, a plateau like non-linear domain appears. ISS values < 50 MPa and \geq 200 MPa were previously determined from push-out tests for HNS and SA3 composites, respectively [20,27]. This work confirmed that HNS cladding composites have a distinguishing feature of low ISS mechanical behavior. For this reinforcement, damaging process saturation (matrix multi-cracking saturation) is rapidly reached (< 200MPa). The consequences observed from unloading reloading cycles are: (i) a rapid decrease of the reduced modulus up to the asymptotic value (**Eq. (2)**), (ii) longitudinal thermal residual strain saturation largely before the ultimate failure and (iii) presence of frictional and sliding mechanisms (proportional to cycles area) occurring earlier. The mechanical behavior of SA3 and SA4 composites are typical of high ISS. Damaging process is more progressive with a delayed reduced modulus decrease, which does not reach the saturation limit, even at very high stress levels (\approx 270MPa for SA4 composites). SA3 composites have slightly higher ISS, as predicted by computation [22,49]. The main difference between SA3 and SA4 composites mechanical behaviors is the much higher failure strain of SA4 composites, similar to HNS composites. It is probably a consequence of the much higher strength of the SA4 fiber in comparison with the SA3 fiber (\approx 30%). Forecasts of average stress-strain behavior of minicomposites for different fiber strengths [49] have demonstrated that composites failure strain is highly dependent on the fiber strength. A 30% decrease in the fiber failure strain could highly reduce the failure strain of composite

(factor 2). This could also explain why erratic failure strains (ranging from 0.15 to 0.6%) for some SA3 minicomposites samples were obtained [20]. Indeed, for small size and unidirectional reinforced composites (25 mm tow length of 800 fibers), it is possible to reach higher failure stress-strain for some tows, leading to a higher failure strain of some samples. This does not occur in complex fibrous structures because they are composed of a large amount of tows.

The Young's modulus (**Table 3**) for all cladding composites type clearly depends on the PyC interphase thickness. Wider standard deviation is also observed for the thickest PyC interphases, which can be related to the wider distribution of the PyC thickness along the samples. **Fig. 11 (a)** reports the tensile stress-strain behavior for 3 SA4/PyC_{250nm}/SiC cladding samples specimens, as a function of their own specific PyC thickness. The tensile modulus is clearly related to the PyC thickness. Indeed, the tensile modulus evolution along with the PyC thickness for all the SA4 composite samples is presented in **Fig. 11 (b)**, confirming the modulus strong dependence on the PyC thickness. For a 300 nm PyC interphase, a strong decrease in the modulus is observed ($\approx 50\%$). The mixed law allows the calculation of estimated composites Young's modulus (E_{est}), without porosity, following **Eq. (4)**:

$$E_{est} = E_f V_f + E_m V_m + E_i V_i \quad (4)$$

With E_f (**Table 1**), E_m (421 GPa) [41], E_i (12 GPa) [14] the fiber, SiC matrix and interphase moduli, respectively. V_f , V_m and V_i the volume fraction of fiber, matrix and interphase, respectively. Rigorously, this formula is only valid for uniaxial CMC (with identical Poisson's ratio). However, it can be a simplified way to estimate the Young's modulus of the different composite materials. Previous studies have tried to evaluate the modulus (E) as a function of porosity volume fraction (P) of ceramic materials [51–54], with **Eq. (5)** and **(6)**.

$$E = E_0 (1 - P)^m \quad (5)$$

$$E = E_0 e^{-bP} \quad (6)$$

where m and b are coefficients describing the modulus dependence on the material porosity. $b = 2.73$ for SiC [51] and $m = 2$ for ceramics (i.e. SiC) without sintering additives and higher with sintering additives or when an external pressure is applied during fabrication [52,54]. Experimental tensile moduli (E_{exp}) are compared with moduli calculated with **Eq. (5)** ($E_{Eq. (5)}$) and **(6)** ($E_{Eq. (6)}$) to account for porosity ($E_0 = E_{est}$). Data from **Table 2** were used to determine E_0 , without taking into account the porosity, i. e. $V_f + V_m + V_i = 1$. Results are presented in **Table 5**. For SA3 and SA4 samples without or with a thin PyC interphase (i.e. ≈ 60 nm), the moduli corrected from porosity ($E_{Eq. (5)}$ and $E_{Eq. (6)}$) are in good agreement with E_{exp} . For thick PyC interphases and for HNS reinforced samples, the estimated moduli are largely higher than the measured one. Therefore, composites modulus with high

ISS and without or with low thickness PyC interphase can be estimated with good agreement by **Eq. (5)** and **(6)**. If the ISS is low (i.e. HNS composite) and/or the PyC is thick, those estimations are not accurate. For such composites, m coefficient should be largely higher than 2 as for ceramics with sintering aids. However, it was not possible to determine it without measurement of the ISS and with only few different interphase thicknesses.

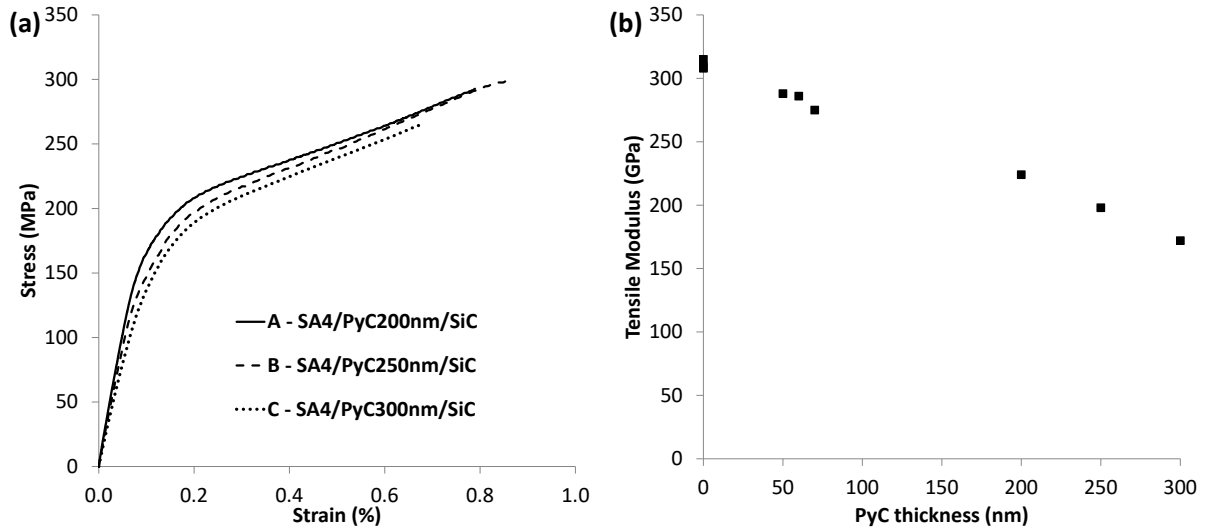


Fig. 11. (a) Tensile stress-strain curves of SA4/PyC_{xxnm}/SiC samples related to their specific PyC thickness (XX = 200, 250 or 300 nm) and (b) Tensile modulus evolution with PyC thickness for SA4 composites cladding samples.

Table 5

Comparison between SiC/SiC cladding experimental Young's modulus (E_{exp}) and estimated moduli, $E_{Eq. (5)}$ and $E_{Eq. (6)}$, corrected from samples porosities with **Eq. (5)** (with $b = 2.73$) and **(6)** (with $m = 2$), respectively. The estimated Young's modulus (E_{est}) is calculated with **Eq. (4)** for a composite without porosities.

Composites	E_{exp} (GPa)	Porosity (%)	E_{est} (GPa)	$E_{Eq. (5)}$ (GPa)	$E_{Eq. (6)}$ (GPa)
SA4/SiC	311	9.9	411	313	333
SA4/PyC _{60nm} /SiC	283	11.6	406	296	317
SA4/PyC _{250nm} /SiC	198	11.4	391	286	307
SA3/PyC _{60nm} /SiC	284	14.9	390	260	282
SA3/PyC _{250nm} /SiC	221	15.0	375	250	272
HNS/PyC _{80nm} /SiC	263	5.2	391	339	351

The PLS follows the same trend than the tensile modulus as a function of ISS and PyC thickness, whatever the method used to determine the PLS (**Table 3**). The higher the ISS value, the higher the PLS for similar interphase thickness. This observation confirms previous simulations and observations [22,48,49]. The novelty of this work is the clear dependence of the PLS on the interphase thickness for these cladding composites. The thinner the interphase, the higher the PLS. This was not observed in previous studies on unidirectional or 2D SiC/SiC composites reinforced with HNS or SA3 fibers mechanically tested in 0° orientation [14,30,55]. The PyC interphase could be assimilated to a softening phase that could allow tailoring the rigidity of composite by adjusting the ISS (modifying the pyrocarbon microstructure and/or extreme surface of fiber) and/or the PyC interphase thickness.

5. Conclusion

In this work, the mechanical behavior of HNS, SA3 and SA4 reinforced cladding composites with different PyC interphase thicknesses was assessed. The similar fibrous structure for all materials allowed easier comparisons. Strong effects of PyC interphase thickness on ISS and Young's modulus have been highlighted. Therefore, significant decrease of Young's modulus for thicker PyC interphases is observed, which can be a result of the PyC interphase acting like secondary phases at grains boundaries in ceramics processed with sintering additives, where such phenomena are observed and already simulated. The breadth of such phenomenon is more important for low ISS composites. This new result could allow engineers to tailor the composites modulus more easily.

Mechanical tensile tests analysis confirms that the new SA4 fiber is clearly an improvement of the previous SA3 fiber. It leads to higher ultimate failure strength mechanical behavior even with thin PyC interphase (necessary for neutron irradiation resistance). The tensile mechanical behavior of SA4 composites is, as for SA3 composites, a distinguish feature of high ISS materials. The SA4 composites behavior is probably the consequence of the SA4 fiber higher tensile strength (comparable to HNS fiber) in comparison with the SA3 fiber. As the ISS is very high in SA4 and SA3 composites, energy transmitted during matrix multi-cracking to the reinforcement is high and tensile strength of fiber is essential to prevent its failure when a crack reaches its surface in order to obtain a pseudo-ductile behavior. SA4 composites have some significant advantages relative to HNS composites for structural applications. PLS of SA4 composites are much higher than HNS composites one, because of their higher ISS. The damaging (matrix multi-cracking and/or opening of existing cracks) of SA4 composites is also largely delayed compared to HNS one. Therefore, SA4 composites are probably more resistant in fatigue at high stress levels. As the degradation is delayed, the reduction of rigidity is also lower for similar stresses. Taking into account that neutron irradiation leads to an ISS decrease, the initially higher ISS in SA4 composites could help to maintain a sufficient ISS under and after neutron irradiation.

This could be a great opportunity to maintain good residual mechanical behavior with sufficient resistance and ductility for high doses. Hence, the new SA4 fiber is of great interest for structural applications and especially for nuclear applications, where HNS fiber demonstrates some serious limitations. The next step will be the processing of samples for environmental corrosion and neutron irradiation experiments to confirm its potential.

6. Acknowledgements

We would like to thank Stephane Le Bras for assistance in mechanical testing and Eric Bouaravong for picture taking of experimental device for tensile tests.

7. References

- [1] C. Sauder, Ceramic Matrix Composites: Nuclear Applications, in: *Ceram. Matrix Compos. Mater. Model. Technol. Appl.*, Narottam P. Bansal and Jacques Lamon, Wiley, Hoboken, NJ, 2014.
- [2] Y. Katoh, L.L. Snead, C.H. Henager, A. Hasegawa, A. Kohyama, B. Riccardi, H. Hegeman, Current status and critical issues for development of SiC composites for fusion applications, *J. Nucl. Mater.* 367–370 (2007) 659–671. <https://doi.org/10.1016/j.jnucmat.2007.03.032>.
- [3] A. Hasegawa, A. Kohyama, R.H. Jones, L.L. Snead, B. Riccardi, P. Fenici, Critical issues and current status of SiC/SiC composites for fusion, *J. Nucl. Mater.* 283–287 (2000) 128–137. [https://doi.org/10.1016/S0022-3115\(00\)00374-3](https://doi.org/10.1016/S0022-3115(00)00374-3).
- [4] Y. Katoh, L.L. Snead, Silicon carbide and its composites for nuclear applications – Historical overview, *J. Nucl. Mater.* 526 (2019) 151849. <https://doi.org/10.1016/j.jnucmat.2019.151849>.
- [5] T. Nozawa, Y. Katoh, L.L. Snead, The effects of neutron irradiation on shear properties of monolayered PyC and multilayered PyC/SiC interfaces of SiC/SiC composites, *J. Nucl. Mater.* 367–370 (2007) 685–691. <https://doi.org/10.1016/j.jnucmat.2007.03.096>.
- [6] Y. Katoh, T. Nozawa, L.L. Snead, T. Hinoki, Effect of neutron irradiation on tensile properties of unidirectional silicon carbide composites, *J. Nucl. Mater.* 367–370 (2007) 774–779. <https://doi.org/10.1016/j.jnucmat.2007.03.083>.
- [7] T. Nozawa, T. Koyanagi, Y. Katoh, H. Tanigawa, High-dose, intermediate-temperature neutron irradiation effects on silicon carbide composites with varied fiber/matrix interfaces, *J. Eur. Ceram. Soc.* 39 (2019) 2634–2647. <https://doi.org/10.1016/j.jeurceramsoc.2019.03.014>.
- [8] S. Suyama, M. Ukai, M. Akimoto, T. Nishimura, S. Tajima, Hydrothermal Corrosion Behaviors of Constituent Materials of SiC/SiC Composites for LWR Applications, *Ceramics*. 2 (2019) 602–611. <https://doi.org/10.3390/ceramics2040047>.
- [9] G. Newsome, L.L. Snead, T. Hinoki, Y. Katoh, D. Peters, Evaluation of neutron irradiated silicon carbide and silicon carbide composites, *J. Nucl. Mater.* 371 (2007) 76–89. <https://doi.org/10.1016/j.jnucmat.2007.05.007>.
- [10] Y. Katoh, T. Nozawa, L.L. Snead, K. Ozawa, H. Tanigawa, Stability of SiC and its composites at high neutron fluence, *J. Nucl. Mater.* 417 (2011) 400–405. <https://doi.org/10.1016/j.jnucmat.2010.12.088>.
- [11] K.A. Terrani, Accident tolerant fuel cladding development: Promise, status, and challenges, *J. Nucl. Mater.* 501 (2018) 13–30. <https://doi.org/10.1016/j.jnucmat.2017.12.043>.
- [12] C.M. Parish, K.A. Terrani, Y.-J. Kim, T. Koyanagi, Y. Katoh, Microstructure and hydrothermal corrosion behavior of NITE-SiC with various sintering additives in LWR coolant environments, *J. Eur. Ceram. Soc.* 37 (2017) 1261–1279. <https://doi.org/10.1016/j.jeurceramsoc.2016.11.033>.
- [13] R. Yamada, N. Igawa, T. Taguchi, Thermal diffusivity/conductivity of Tyranno SA fiber- and Hi-Nicalon Type S fiber-reinforced 3-D SiC/SiC composites, *J. Nucl. Mater.* 329–333 (2004) 497–501. <https://doi.org/10.1016/j.jnucmat.2004.04.109>.
- [14] Y. Katoh, T. Nozawa, L.L. Snead, T. Hinoki, A. Kohyama, Property tailorability for advanced CVI silicon carbide composites for fusion, *Fusion Eng. Des.* 81 (2006) 937–944. <https://doi.org/10.1016/j.fusengdes.2005.08.045>.
- [15] J.J. Sha, T. Nozawa, J.S. Park, Y. Katoh, A. Kohyama, Effect of heat treatment on the tensile strength and creep resistance of advanced SiC fibers, *J. Nucl. Mater.* 329–333 (2004) 592–596. <https://doi.org/10.1016/j.jnucmat.2004.04.123>.
- [16] W. Yang, H. Araki, A. Kohyama, Q. Yang, T. Noda, Effects of heat treatment on the microstructure and flexural properties of CVI–Tyranno–SA/SiC composite, *Ceram. Int.* 33 (2007) 141–146. <https://doi.org/10.1016/j.ceramint.2005.08.011>.
- [17] N. Igawa, T. Taguchi, L.L. Snead, Y. Katoh, S. Jitsukawa, A. Kohyama, J.C. McLaughlin, Optimizing the fabrication process for superior mechanical properties in the FCVI SiC matrix/stoichiometric SiC fiber composite system, *J. Nucl. Mater.* 307–311 (2002) 1205–1209. [https://doi.org/10.1016/S0022-3115\(02\)01060-7](https://doi.org/10.1016/S0022-3115(02)01060-7).

- [18] B. Riccardi, E. Trentini, M. Labanti, M. Leuchs, S. Roccella, E. Visca, Characterization of commercial grade Tyranno SA/CVI-SiC composites, *J. Nucl. Mater.* 367–370 (2007) 672–676. <https://doi.org/10.1016/j.jnucmat.2007.03.098>.
- [19] K. Ozawa, T. Nozawa, Y. Katoh, T. Hinoki, A. Kohyama, Mechanical properties of advanced SiC/SiC composites after neutron irradiation, *J. Nucl. Mater.* 367–370 (2007) 713–718. <https://doi.org/10.1016/j.jnucmat.2007.03.033>.
- [20] C. Sauder, A. Brusson, J. Lamon, Influence of interface characteristics on the mechanical properties of Hi-Nicalon type-S or Tyranno-SA3 fiber-reinforced SiC/SiC minicomposites: influence of interface characteristics on the mechanical properties, *Int. J. Appl. Ceram. Technol.* 7 (2010) 291–303. <https://doi.org/10.1111/j.1744-7402.2010.02485.x>.
- [21] C. Fellah, J. Braun, C. Sauder, F. Sirotti, M.-H. Berger, Influence of the carbon interface on the mechanical behavior of SiC/SiC composites, *Compos. Part Appl. Sci. Manuf.* 133 (2020) 105867. <https://doi.org/10.1016/j.compositesa.2020.105867>.
- [22] L. Li, Z. Zhang, Y. Liu, Effect of interface properties on the nonlinear behaviour of long-fibre-reinforced unidirectional ceramic-matrix mini-composites subjected to tensile and fatigue loading, *Ceram. - Silik.* 64 (2020) 348–364. <https://doi.org/10.13168/cs.2020.0023>.
- [23] Y. Katoh, S.M. Dong, A. Kohyama, Thermo-mechanical properties and microstructure of silicon carbide composites fabricated by nano-infiltrated transient eutectoid process, *Fusion Eng. Des.* 61–62 (2002) 723–731. [https://doi.org/10.1016/S0920-3796\(02\)00180-1](https://doi.org/10.1016/S0920-3796(02)00180-1).
- [24] W. Yang, T. Noda, H. Araki, J. Yu, A. Kohyama, Mechanical properties of several advanced Tyranno-SA fiber-reinforced CVI-SiC matrix composites, *Mater. Sci. Eng. A.* 345 (2003) 28–35. [https://doi.org/10.1016/S0921-5093\(02\)00468-9](https://doi.org/10.1016/S0921-5093(02)00468-9).
- [25] W. Yang, H. Araki, A. Kohyama, H. Suzuki, T. Noda, Effects of SiC sub-layer on mechanical properties of Tyranno-SA/SiC composites with multiple interlayers, *Ceram. Int.* 31 (2005) 525–531. <https://doi.org/10.1016/j.ceramint.2004.06.018>.
- [26] K. Shimoda, A. Kohyama, T. Hinoki, High mechanical performance SiC/SiC composites by NITE process with tailoring of appropriate fabrication temperature to fiber volume fraction, *Compos. Sci. Technol.* 69 (2009) 1623–1628. <https://doi.org/10.1016/j.compscitech.2009.03.011>.
- [27] E. Buet, C. Sauder, D. Sornin, S. Poissonnet, J.-N. Rouzaud, C. Vix-Guterl, Influence of surface fibre properties and textural organization of a pyrocarbon interphase on the interfacial shear stress of SiC/SiC minicomposites reinforced with Hi-Nicalon S and Tyranno SA3 fibres, *J. Eur. Ceram. Soc.* 34 (2014) 179–188. <https://doi.org/10.1016/j.jeurceramsoc.2013.08.027>.
- [28] E. Buet, C. Sauder, S. Poissonnet, P. Brender, R. Gadiou, C. Vix-Guterl, Influence of chemical and physical properties of the last generation of silicon carbide fibres on the mechanical behaviour of SiC/SiC composite, *J. Eur. Ceram. Soc.* 32 (2012) 547–557. <https://doi.org/10.1016/j.jeurceramsoc.2011.09.023>.
- [29] T. Koyanagi, Y. Katoh, T. Nozawa, Design and strategy for next-generation silicon carbide composites for nuclear energy, *J. Nucl. Mater.* 540 (2020) 152375. <https://doi.org/10.1016/j.jnucmat.2020.152375>.
- [30] Y. Katoh, K. Ozawa, C. Shih, T. Nozawa, R.J. Shnavski, A. Hasegawa, L.L. Snead, Continuous SiC fiber, CVI SiC matrix composites for nuclear applications: Properties and irradiation effects, *J. Nucl. Mater.* 448 (2014) 448–476. <https://doi.org/10.1016/j.jnucmat.2013.06.040>.
- [31] Y. Katoh, T. Nozawa, C. Shih, K. Ozawa, T. Koyanagi, W. Porter, L.L. Snead, High-dose neutron irradiation of Hi-Nicalon Type S silicon carbide composites. Part 2: Mechanical and physical properties, *J. Nucl. Mater.* 462 (2015) 450–457. <https://doi.org/10.1016/j.jnucmat.2014.12.121>.
- [32] S. Kondo, T. Hinoki, M. Nonaka, K. Ozawa, Irradiation-induced shrinkage of highly crystalline SiC fibers, *Acta Mater.* 83 (2015) 1–9. <https://doi.org/10.1016/j.actamat.2014.07.057>.
- [33] T. Koyanagi, T. Nozawa, Y. Katoh, L.L. Snead, Mechanical property degradation of high crystalline SiC fiber-reinforced SiC matrix composite neutron irradiated to ~100 displacements per atom, *J. Eur. Ceram. Soc.* 38 (2018) 1087–1094. <https://doi.org/10.1016/j.jeurceramsoc.2017.12.026>.

- [34] A. Seshadri, B. Philips, A.J. Dave, S. Harrison, J. Pegna, K. Shirvan, Hydrothermal corrosion of laser printed SiC fibers under extreme environment, *J. Nucl. Mater.* 548 (2021) 152805. <https://doi.org/10.1016/j.jnucmat.2021.152805>.
- [35] D. Kim, H.J. Lee, C. Jang, H.-G. Lee, J.Y. Park, W.-J. Kim, Influence of microstructure on hydrothermal corrosion of chemically vapor processed SiC composite tubes, *J. Nucl. Mater.* 492 (2017) 6–13. <https://doi.org/10.1016/j.jnucmat.2017.05.010>.
- [36] J.H. Shin, D. Kim, H.-G. Lee, J.Y. Park, W.-J. Kim, Factors affecting the hydrothermal corrosion behavior of chemically vapor deposited silicon carbides, *J. Nucl. Mater.* 518 (2019) 350–356. <https://doi.org/10.1016/j.jnucmat.2019.03.026>.
- [37] Y. Qin, X. Li, C. Liu, C. Zheng, Q. Mao, B. Chen, K. Jing, Y. Tan, L. Cheng, L. Zhang, Effect of deposition temperature on the corrosion behavior of CVD SiC coatings on SiCf/SiC composites under simulated PWR conditions, *Corros. Sci.* 181 (2021) 109233. <https://doi.org/10.1016/j.corsci.2020.109233>.
- [38] S.M. Dong, G. Chollon, C.L.E. Re, M. Lahaye, A. Guette, J.L. Bruneel, M. Couzi, R. Naslain, D.L. Jiang, Characterization of nearly stoichiometric SiC ceramic fibres, *J. Mater. Sci.* 36 (2001) 2371–2381. <https://doi.org/10.1023/A:1017988827616>.
- [39] C. Sauder, J. Lamon, Tensile creep behavior of SiC-based fibers with a low oxygen content, *J. Am. Ceram. Soc.* 90 (2007) 1146–1156. <https://doi.org/10.1111/j.1551-2916.2007.01535.x>.
- [40] J. Braun, C. Sauder, J. Lamon, F. Balbaud-Célérier, Influence of an original manufacturing process on the properties and microstructure of SiC/SiC tubular composites, *Compos. Part Appl. Sci. Manuf.* 123 (2019) 170–179. <https://doi.org/10.1016/j.compositesa.2019.04.031>.
- [41] A. Michaux, C. Sauder, G. Camus, R. Pailler, Young's modulus, thermal expansion coefficient and fracture behavior of selected Si–B–C based carbides in the 20–1200°C temperature range as derived from the behavior of carbon fiber reinforced microcomposites, *J. Eur. Ceram. Soc.* 27 (2007) 3551–3560. <https://doi.org/10.1016/j.jeurceramsoc.2006.12.006>.
- [42] ISO 20323, Fine ceramics (advanced ceramics, advanced technical ceramics) - Mechanical properties of ceramic composites at ambient temperature in air atmospheric pressure - Determination of tensile properties of tubes, 2018.
- [43] M.G. Jenkins, L.P. Zawada, Elastic Modulus and Proportional Limit Stress in Ceramic Matrix Composites: Comparison of Methods and Results, in: 25th Annu. Conf. Compos. Adv. Ceram. Mater. Struct. Ceram. Eng. Sci. Proc., John Wiley & Sons, Ltd, 2001: pp. 502–511. <https://doi.org/10.1002/9780470294680.ch58>.
- [44] G. Camus, L. Guillaumat, S. Baste, Development of damage in a 2D woven C/SiC composite under mechanical loading: I. Mechanical characterization, *Compos. Sci. Technol.* 56 (1996) 1363–1372. [https://doi.org/10.1016/S0266-3538\(96\)00094-2](https://doi.org/10.1016/S0266-3538(96)00094-2).
- [45] S. Baste, Inelastic behaviour of ceramic-matrix composites, *Compos. Sci. Technol.* 61 (2001) 2285–2297. [https://doi.org/10.1016/S0266-3538\(01\)00122-1](https://doi.org/10.1016/S0266-3538(01)00122-1).
- [46] J.-M. Domergue, E. Vagaggini, A.G. Evans, Relationships between Hysteresis Measurements and the Constituent Properties of Ceramic Matrix Composites: II, Experimental Studies on Unidirectional Materials, *J. Am. Ceram. Soc.* 78 (1995) 2721–2731. <https://doi.org/10.1111/j.1151-2916.1995.tb08047.x>.
- [47] C.S. Lynch, A.G. Evans, Effects of Off-Axis Loading on the Tensile Behavior of a Ceramic-Matrix Composite, *J. Am. Ceram. Soc.* 79 (1996) 3113–3123. <https://doi.org/10.1111/j.1151-2916.1996.tb08085.x>.
- [48] A.G. Evans, F.W. Zok, The physics and mechanics of fibre-reinforced brittle matrix composites, *J. Mater. Sci.* 29 (1994) 3857–3896. <https://doi.org/10.1007/BF00355946>.
- [49] N. Lissart, J. Lamon, Damage and failure in ceramic matrix minicomposites: Experimental study and model, *Acta Mater.* 45 (1997) 1025–1044. [https://doi.org/10.1016/S1359-6454\(96\)00224-8](https://doi.org/10.1016/S1359-6454(96)00224-8).
- [50] M. Bouquet, J.M. Birbis, J.M. Quenisset, Toughness assessment of ceramic matrix composites, *Compos. Sci. Technol.* 37 (1990) 223–248. [https://doi.org/10.1016/0266-3538\(90\)90102-B](https://doi.org/10.1016/0266-3538(90)90102-B).

- [51] R. Ruh, A. Zangvil, J. Barlowe, Elastic Properties of SiC, AlN, and Their Solid Solutions and Particulate Composites, 64 (1985) 7.
- [52] A.S. Wagh, R.B. Poeppel, J.P. Singh, Open pore description of mechanical properties of ceramics, J. Mater. Sci. 26 (1991) 3862–3868. <https://doi.org/10.1007/BF01184983>.
- [53] C. Reynaud, F. Thévenot, T. Chartier, J.-L. Besson, Mechanical properties and mechanical behaviour of SiC dense-porous laminates, J. Eur. Ceram. Soc. 25 (2005) 589–597. <https://doi.org/10.1016/j.jeurceramsoc.2004.02.009>.
- [54] K.S. Blanks, A. Kristoffersson, E. Carlström, W.J. Clegg, Crack Deflection in Ceramic Laminates Using Porous Interlayers, J. Eur. Ceram. Soc. 18 (1998) 1945–1951. [https://doi.org/10.1016/S0955-2219\(98\)00134-4](https://doi.org/10.1016/S0955-2219(98)00134-4).
- [55] T. Hinoki, E. Lara-Curzio, L.L. Snead, Mechanical Properties of High Purity SiC Fiber-Reinforced CVI-SiC Matrix Composites, Fusion Sci. Technol. 44 (2003) 211–218. <https://doi.org/10.13182/FST03-A336>.